Article

Fluid Dynamic and Thermal Performance of a V-Shape Slotted Cylinder

Abdulwahab Alhashem *, Sultan Alshareef, Ali Y. Alharbi [ID] and Mosab A. Alrahmani [ID]

Department of Mechanical Power & Refrigeration Technology, College of Technological Studies, The Public Authority for Applied Education and Training, Kuwait City 70654, Kuwait; sm.alshareef@paaet.edu.kw (S.A.); ay.alharbi@paaet.edu.kw (A.Y.A.); ma.alrahmani@paaet.edu.kw (M.A.A.)
* Correspondence: ai.alhashem@paaet.edu.kw

Abstract: The flow characteristics and thermal performance of circular cylinders with V-shape slots are investigated numerically. The simulation is a two-dimensional incompressible flow that employs the semi-implicit finite volume multi-material algorithm MPM-ICE, which is a module of the Uintah framework. The normalized slot width s_2/D ranges from 0.1 to 0.2, and the corresponding increases in total surface area are from ~99% to ~70%, respectively. Compared to the solid cylinder, the slotted cylinder has the largest total drag reduction of ~67% at s_2/D of 0.2. Meanwhile, although the heat transfer is proportional with the surface area, the thermal performance of the V-shape slot first improves with the slot width, and then declines. The heat transfer improvement has an optimum value of ~192% at s_2/D of 0.15. The overall slot performance, defined by the ratio of the heat transfer to the drag force, is best at 0.175.

Keywords: pin fin; fin thermal performance; slotted fin; heat sink; air cooled; forced convection

1. Introduction

The advancements in materials fabrication and manufacturing technologies enable thermal systems to function in high-temperature environments and achieve higher rates of heat transfer. Enhancing convective heat transfer is crucial for improving thermal performance and increasing the reliability of systems. An effective technique involves incorporating extended surfaces on the heat transfer area, a common practice in various engineering applications. Pin fins are essential in gas turbine technology to cool turbine blades, thereby improving turbine efficiency and durability [1]. On a small scale, the heat flux requirements increased to 520 W/cm^2 for electronic chips in 2011 [2], and approximately 10^3 W/cm^2 for supercomputers, electric motors, and power devices [3]. Pin fins are commonly employed in various electronic devices to enhance system reliability. This is because around 55% of electronic failures occur when the system operates at temperatures that exceed their intended operating temperature [4].

The growing need to improve thermal performance and address reliability concerns has led to the exploration of various advanced cooling techniques, including spray cooling, jet impingement, air cooling, liquid cooling, pool and flow boiling, nanofluid cooling, and others [3–8]. Although each method has its level of success and value, the main difficulty lies in clearly defining possible enhancements. Out of all the methods available, air-forced convection is still considered appealing due to its simplicity and low cost. However, there is still ongoing debate about its ability to reach the desired thermal capacity [9].

Heat sinks utilizing extended surfaces such as pin fins and plate fins are renowned for their significant enhancement in thermal performance. They are particularly useful in situations where there are limitations on weight and size. Extensive research has been carried out on the arrangement, spacing, and flow conditions of fins [2–11]. In addition, there has been significant research conducted on various pin fin geometries, including round, triangular, quadrilateral, elliptical, dropform, and others [2–11]. Additional research

has explored innovative options such as unique fin shapes, fluid additives, flow barriers, surface irregularities, and other factors. Furthermore, advancements have been made by introducing flow disturbances to improve heat transfer while various techniques, thoroughly elucidated in the literature, continue to be of interest whenever there is potential for enhancement [2–11].

Numerous studies have examined techniques for regulating and enhancing the flow around cylinders. One approach is to mitigate vortex-induced vibration (VIV), which is influenced by the regularity of vortex shedding. Techniques for improvement can be categorized as either active or passive [12]. Experimental studies have been conducted on passive flow control techniques, such as the integration of slots [13–18]. These studies examined the effects of various flow conditions, including the normalized slot width s/D, Reynolds number Re, and incident angle β. The primary aim of these experiments was to investigate the impact of the slot on the drag and lift forces. The maximum reduction in drag coefficient occurs when $\beta \leq 40°$, primarily because of the increase in base pressure. Moreover, the implementation of a slot plays a crucial role in minimizing the effects of induced vibration by effectively moving the wake at a greater distance from the cylinder. While there has been a focus on the fluid dynamics of slotted cylinders in experimental research, no studies have been found that specifically examine the heat transfer characteristics.

Several numerical studies have been conducted on the flow over slotted cylinders, with a primary focus on fluid dynamics [19–25]. The work encompassed various parameters such as Re, s/D, and β, which were analyzed to determine their influence on dynamic forces. The results obtained from numerical simulations align closely with the results obtained from experimental work. Heat transfer-wise, a computational study was conducted to analyze the thermal performance of slotted cylinders used for electronic cooling [26]. The study investigates the impact of β, cylinder aspect ratio, and blockage ratio on Re values ranging from 26 to 260. The findings indicate that the highest level of performance is achieved when the aspect ratio is 0.3, and the thermal performance improves as the blockage ratio increases. Furthermore, a comparison was made between an array of slotted micropillars and non-slotted pillars. The study determined that the temperature of the heated wall was decreased by an additional 7.2 °C when slotted pillars were used.

Jadon and Arumuru [27] conducted a numerical analysis on cylinders with slots positioned at an angle of $\beta = 0°$, which were placed between two parallel plates. The study investigated the impact of slot size relative to the cylinder's diameter (Re_D), ranging from 60 to 240. The study validates the possibility of increased heat transfer compared to a solid cylinder. The results demonstrate a significant decrease in C_D (drag coefficient) and C_L (lift coefficient) as the values of s/D and Re_D increase. Furthermore, the increase in heat transfer on the curved surface is more pronounced when the ratio of the surface area to the hydraulic diameter (s/D) and the Reynolds number (Re_D) are larger, as indicated by the local Nusselt number (Nu). Furthermore, the time-averaged Nusselt number (Nu) for both the outside curved surface and the internal slot surface exhibits a rise as the ratio of s/D and the Reynolds number (Re_D) increase. All cases in the performance index have a value above one, indicating a favorable outcome. However, the highest performance was found for the s/D ratio within the range of 0.2–0.25.

In their study, Hsu [28] conducted numerical simulations to examine the impact of slot inclination on heat transfer around a cylinder. The slot had a width of $s/D = 0.1$, and the Reynolds number (Re_D) ranged from 100 to 500. The study demonstrates that the injection mode at an angle of $\beta = 0°$ is more efficient in enhancing heat transfer compared to the blowing/suction mode. The averaged Nusselt number on the external surface is higher than that for the slot when the Reynolds number is less than or equal to 200 because the flow rate within the slot is low.

A recent study examined two slotted cylinder configurations, parallel slots, and orthogonal slots for heat transfer enhancement in aligned flow [29]. The arrangement of the parallel slots increased the slot mass flow rate, but the mass flow rate decreased as the separation distance increased. The configuration of the orthogonal slots enhanced

rear curved surface heat transfer, but the total curved surface thermal performance was less than a single slot. Overall, positive thermal and overall performance was found. Another study by Alshareef [30] reveals that a single slot on a two-dimensional ellipsoid significantly impacts bluff bodies, reducing drag force and heat transfer rate. The bluff body experiences higher total drag force reduction and heat transfer enhancement compared to streamlined bodies. Additionally, bluff bodies have less additional irreversibility compared to streamlined bodies for Reynolds numbers $\geq$ 400 and 1000, with less total entropy generation. Finally, Alshareef's study [31] suggests that a fin with a slot surface in parallel with the inward flow can improve the thermal performance of heat sink device systems by up to 70%. This leads to an increased total heat rate and an overall performance index of up to three. Correlations for Nu and C_D are proposed, along with an optimized flow condition correlation. The asymptotic thermal performance plateaus around $Re_D \sim 500$ for most of the s/D cases where all the slots are oriented in parallel to the incoming flow [31]. Overall, the optimal s/D width for the cases studied on fins with slots parallel to the incoming flow ranged between 0.2 and 0.25 [27,31]. Numerical and experimental work in the literature on circular pin fins are summarized in Table 1, showing the studied conditions and remarks.

Table 1. The literature review on slotted cylinders with circular cross-section.

Author	Study Type	Configuration	Conditions	Remark	
Alshareef et al. [31]	Numerical Fluid dynamic and heat transfer	Circular cylinder with horizontal slot	Re range 100–1000 s/D range 0.1–0.3	-	Up to ~45% drag reduction. Up to ~70% thermal enhancement.
Jadon and Arumuru [27]	Numerical Fluid dynamic and heat transfer	Circular cylinder with a slit paralell to flow direction	Re range 60–240 s/D range 0–0.25	-	16% drag reduction. 10% increase in average Nu for s/D = 0.25.
Hsu [28]	Numerical Fluid dynamic and heat transfer	Two circular cylinders with slotted located upstream	Re: 100 and 200 s/D = 0.1	-	Array Nu enhancement ranged between 6–15%. The optimal slit orientation angle was found to be 45°–60°.
Baek and Karniadakis [19]	Experimental. Fluid dynamic	Circular cylinder with horizontal slot	s/D range 0–0.3 Re: 500 and 1000	-	Up to ~40% drag reduction at Re = 500.
Wang and Dong [22]	Experimental Fluid dynamic and heat transfer	Circular cylinder: Solid and slotted with 82° angle	s/D range 0.02–0.1 Re = 225 for slotted cylinder.	-	Thermal enhancement with slot width.
Zhenzhong et al. [24]	Experimental Fluid dynamic	Circular cylinder: Solid and inclined slot	s/D range 0–0.3 $0 \leq \beta \leq 90°$ Re = 200	-	For $0 \leq \beta \leq 45°$, drag reduction of 28.6% at s/D = 0.3 and β = 0. For $45 \leq \beta \leq 60°$, drag force gradually exceeds that of solid cylinder.
Mishra and Hanzla [25]	Numerical Fluid dynamic	Circular cylinder: Solid and inclined slot	s/D range 0.05–0.25 $0 \leq \beta \leq 90°$	-	Up to ~32% drag reduction at Re = 47 and β = 0.

Examining the fluid dynamic around fins helps to define ways to reduce the drag force on slotted cylinders, which lessens the required pumping power. In addition, enhancing the thermal performance allows more heat removal, which is better for heat sink applications, and it reduces material size for the case of a fixed heat rate. While numerical studies are abundant in fluid dynamics investigations, previous numerical studies on thermal characteristics are still limited. In addition, while previous numerical studies explicate the thermal benefits of cylindrical fins with a slot, the configurations studied were restricted to a few slot orientations.

The current study proposes a new slot design, not reported in the literature, to replace the traditional solid pin fins. This paper specifically examines the airflow generated by conventional methods over a pin fin with a circular cross-section. The design incorporates a horizontally oriented V-shaped slot aligned with the direction of airflow. It features a single entrance and two exits for the air. The current study takes into consideration the optimal

Re_D of 500 and s/D of 0.2 suggested by Alshareef [31]. The V-shaped slot has a fixed width at the inlet, $s_1 = 0.2D$, while the other two inner slots at the exit have a variable width of $0.1D \leq s_2 \leq 0.2D$. A numerical analysis is conducted to evaluate the fluid dynamics and thermal efficiency of the slotted fin. This study aims to evaluate the impact of the designated slot configuration on the drag force and heat transfer. The proposed slot is also expected to reduce the fluid dynamics forces on the fin in a similar manner to conventional parallel slots.

2. Methodology

The present study employs the MPM-ICE algorithm from the Uintah framework [32]. This algorithm is a continuum-based, multifield, compressible, unsteady, Eulerian–Lagrangian fluid–structure interaction (FSI) algorithm that utilizes a Cartesian structured grid. It allows for the independent or simultaneous modeling of fluids, represented by ICE (implicit, continuous fluid, Eulerian) characteristics, and solid materials, represented by the MPM (material point method). Detailed algorithm descriptions, including the governing equations and other pertinent information, can be found in reference [32]. Essentially, the algorithm employs a multifield approach in which materials are consistently defined across the entire domain, and interactions between them are facilitated by closure models within the governing equations that exchange momentum and energy. retain

This approach offers a significant advantage, as it closely connects the physics by means of the conservation equations, thereby eliminating the requirement to establish boundary conditions at the interfaces between the fluid and solid. The conservation of mass, momentum, and internal energy are given in Equations (1)–(3). They are derived from an algorithm excluding phase change, turbulence, combustion, and gravity effects.

$$\frac{\partial \rho_i}{\partial t} + \nabla \cdot (\rho \boldsymbol{u})_i = 0 \tag{1}$$

$$\frac{\partial (\rho \boldsymbol{u})_i}{\partial t} + \nabla \cdot (\rho \boldsymbol{u} \boldsymbol{u})_i = -\theta_i \nabla P + \nabla \cdot (\theta \boldsymbol{\tau})_i + \sum_{j=1}^{N} f_{ij} \tag{2}$$

$$\frac{\partial (\rho e)_i}{\partial t} + \nabla \cdot (\rho e \boldsymbol{u})_i = -\frac{P \theta_i}{v_i} \frac{dv_i}{dt} + (\theta \boldsymbol{\tau})_i : \nabla \boldsymbol{u}_i + \nabla \cdot (\theta k \nabla T)_i + \sum_{j=1}^{N} q_{ij} \tag{3}$$

The MPM-ICE algorithm employs the momentum and energy exchange closure models, represented by the third and fourth terms in Equations (2) and (3), respectively, to account for interactions between multiple materials. The models f_{ij} and q_{ij} denote the force and energy transferred per unit volume of material i as a result of its interaction with material j, per unit volume of material i. Equations (4) and (5) represent these models, respectively.

$$\sum_{j=1}^{N} f_{ij} = \sum_{j=1}^{N} K_{ij} \theta_i \theta_j (\boldsymbol{u}_j - \boldsymbol{u}_i) \tag{4}$$

$$\sum_{j=1}^{N} q_{ij} = \sum_{j=1}^{N} H_{ij} \theta_i \theta_j (T_j - T_i) \tag{5}$$

Given the absence of a clear separation between fluid and solid in MPM-ICE, there is no need for boundary conditions at the fluid–solid interfaces. However, it is still necessary to maintain momentum and energy equilibrium between the materials. The flow simulated in the study is within the continuum regime, where the Knudsen number is relatively small ($Kn << 1$), and the Navier–Stokes equation can be solved using the no-slip velocity at the wall. The isothermal surface temperature around the perimeter of the cylinder is a typical boundary condition for pin fins in a heat sink system where the radial temperature gradient is negligible due to the small value of the Biot number ($Bi << 1$). The implementation of no-slip and isothermal conditions at the fluid–solid interface, specifically the cylinder walls, is achieved by utilizing the momentum and energy exchange coefficients, K_{ij} and H_{ij}. These coefficients are assigned to extremely high values, typically around 10^{15}, to resemble the proper fluid boundary condition at the wall/surface [32]. This forces the two materials

to possess identical velocity (no slip) and temperature (no temperature jump) within the cell where the surface is identified (fluid–solid interface), as these two parameters play a significant role on the flow patterns, lift and drag forces, and the heat transfer rate. Greater values of K_{ij} and H_{ij} indicate a more pronounced interaction or exchange between materials, and they function as a boundary condition at the interface between a fluid and a solid. The Dirichlet–Neumann boundary conditions are applied to all the edges of the domain in a manner consistent with that used in commercial codes, as depicted in Figure 1a. It should be noted that Equations (3) and (4) are solved using a cell-wise implicit method [30–33].
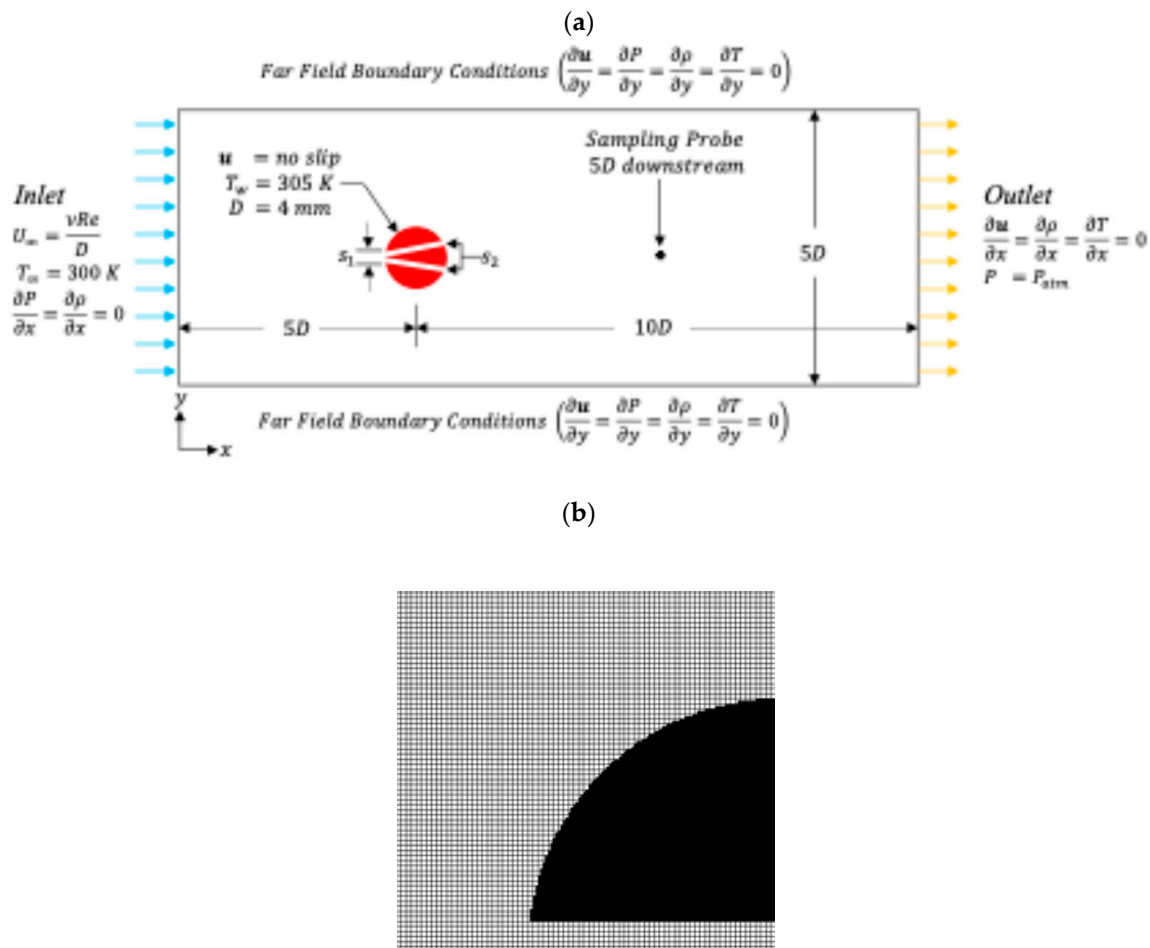
(a)

(b)

Figure 1. Numerical details: (**a**) problem setup and (**b**) mesh quality (coarsest mesh) of the upper half of a cylinder with a horizontal slot with constant width of $s/D = 0.1$ [31].

3. Problem Statement and Simulation Details

The present study examines the airflow over stationary circular/slotted cylinders with a constant surface temperature in a two-dimensional setting. The airflow is presumed to be incompressible, with no phase change, and in the continuum regime, it has a maximum Mach number of approximately 0.005, indicating a Reynolds number of 500, and exhibiting laminar flow behavior. The thermophysical fluid properties are assumed to be constant, except for temperature and pressure. These properties are determined based on their values at $T = 300$ K and $P = 1$ atm. The Prandtl number (Pr) is 0.71, the dynamic viscosity (μ) is 1.846×10^{-5} Pa·s, the thermal conductivity (k) is 0.0263 W/(m·K), the density (ρ) is 1.1614 kg/m^3, and the specific heat capacity (c_p) is 1007 J/(kg·K). The properties of the cylinder correspond to those of copper at a temperature of 305 K. The circular disk is at a constant temperature, and the change in temperature with respect to the distance from the center is negligible ($\partial T/\partial r = 0$). This means that solving the heat conduction equation within the solid material is not required. The conditions are set so there is no influence on

the accuracy of the simulations. The Reynolds number, denoted as Re_D, is calculated using Equation (6).

$$Re_D = \mu U_\infty D / \rho \tag{6}$$

In this study, the Reynolds number is 500. The ratio of the normalized slot width (s_2/D) ranges from 0.1 to 0.2, increasing by increments of 0.025, while the inlet slot size is set at a constant, $s_1/D = 0.2$. The increased surface area of the proposed V-shaped slots ranges from 98.9% to 69.5% for s_2/D values of 0.1 and 0.2, respectively, in comparison to the surface area of the solid cylinder ($s/D = 0$).

The cumulative force (viscous and pressure) and the total heat transfer rate for all cases are calculated using a control volume analysis across the entire specified domain. This analysis was conducted at a frequency of 10^5 Hz (every 0.01 milliseconds). The flow demonstrated periodic behavior within the examined Re_D. As a result, all relevant quantities of interest (*qoi*), including the drag coefficient C_D and lift coefficient C_L, shown in Equations (7) and (8), respectively, the total drag force F_d, total heat rate Q, and total Nusselt number Nu, shown in Equation (9), and where ΔT is shown in Equation (10), were averaged over time once the flow field achieved a periodic steady state. The frontal areas, denoted as $A_f = DL_z$, for the solid and slotted cylinders, do not include the surface area of the slot. The surface area A_{cyl} for the solid cylinder is defined as πDL_z.

$$C_D = 2F_d / (\rho_\infty U_\infty^2 A_f) \tag{7}$$

$$C_L = 2F_L / (\rho_\infty U_\infty^2 A_f) \tag{8}$$

$$Nu = QD / (A_{cyl} k \Delta T) \tag{9}$$

$$\Delta T = T_w - T_\infty \tag{10}$$

The study determined that the domain details, including the size of the domain, the lengths of the upstream, downstream, and transverse sections, and the boundary conditions depicted in Figure 1a, were sufficient for this investigation [33,34]. The fundamental field variables, specifically pressure, temperature, velocity, and density are set to their initial values using the freestream values.

3.1. Grid Independent Study

Prior MPM-ICE simulations of a cylinder in crossflow led to the conclusion that a cell spatial discretization of $D/16$ is sufficient for achieving a reasonably accurate Strouhal number [33,34]. Since the internal flow within the slot requires much grid refinement to capture the flow field characteristics, and since the smallest slot size for the study was $s_2 = 0.1D$, a finer mesh than $D/16$ is required. The grid independence study conducted by Alshareef [31] used the setting of a horizontal slotted cylinder with a constant slot width along the cylinder of $s/D = 0.1$ at $Re_D = 1000$. This should be more inclusive, as the higher $Re_D = 1000$ is twice that in the current study investigation. The grid independence study is conducted by varying the resolution, specifically by altering the number of grid cells within the slot. The coarse mesh depicted in Figure 1b, referred to as h_3, consisted of 10 cells in the transverse direction, which is equivalent to $D/100$. The medium and fine meshes, h_2 and h_1, have 20 and 40 cells across the slot, corresponding to $D/200$ and $D/400$, respectively. The dimensions of the cells, $\Delta x = \Delta y = \Delta z$, corresponding to $D/100$, $D/200$, and $D/400$, are 40 μm, 20 μm, and 10 μm, respectively, when D is equal to 4 mm. The simulation of the fine mesh case required extensive computational resources, where 512 cores were utilized for approximately ~216 h.

The grid independence study is performed using a consistent time step for all resolutions that was based on the Courant–Friedrichs–Lewy number (*CFL*). The *CFL* values for the $D/100$, $D/200$, and $D/400$ cases were 0.10625, 0.2125, and 0.85, respectively. The pressure Poisson equation is solved with a convergence criterion of 10^{-10} and 10^{-12} for the inner and outer iterations of the pressure solver, respectively. The solution adopts the

pfmg preconditioner from the hyper library. The maximum outer iterations are set to 10. The simulations continue until reaching a state of steady periodicity or completing ten system flushes. To facilitate the visualization of the flow field, a passive scalar (dye) is introduced at the entrance of the domain and transported throughout the entire domain. The dye is observed to verify that there is no non-physical movement at the boundaries of the domain. Observing the temporal evolution of the coefficients of drag (C_D) and lift (C_L) also verifies the absence of reverse flow at the outlet. The quantity of interest, *qoi*, is the total heat transfer rate represented by *Nu*.

The grid independence study was performed using the grid convergence index (*GCI*) method, as suggested by Roache [35]. This method is known for its conservative approach to error estimation compared to others. The *GCI* formula for the medium and fine mesh is given by Equations (11) and (12), respectively, where *FS* represents the factor of safety, *r* denotes the grid refinement ratio, and p_{obs} represents the observed order of accuracy.

$$GCI_{medium} = FS \ |(qoi_2 - qoi_3)/qoi_2| / (r^{pobs} - 1) \tag{11}$$

$$GCI_{fine} = FS \ |(qoi_1 - qoi_2)/qoi_1| / (r^{pobs} - 1) \tag{12}$$

On the other hand, for the coarse mesh, the *GCI* is calculated as shown in Equation (13). Table 2 and Figure 2 display the quantity of interest (*qoi*) and the grid convergence index values for each normalized resolution, *R** [31]. The data suggest that quantity of interest (*qoi*) value converges in a monotonous manner. This is determined by calculating the monotonic convergence index, *R*, as shown in Equation (14), which ranges from 0 to 1. The spatial theoretical order of accuracy of MPM-ICE is second order. The grid independence study indicates that for the present study, the observed order of accuracy, p_{obs}, which is calculated using Equation (15), is ~2.24.

$$GCI_{coarse} = FS \ r^{pobs} \ |(qoi_1 - qoi_2)/qoi_1| / (r^{pobs} - 1) \tag{13}$$

$$R = (qoi_1 - qoi_2)/(qoi_2 - qoi_3) \tag{14}$$

$$p_{obs} = |\ln((qoi_3 - qoi_2)/(qoi_2 - qoi_1))| / \ln(r) \tag{15}$$

Table 2. GCI study summary [31].

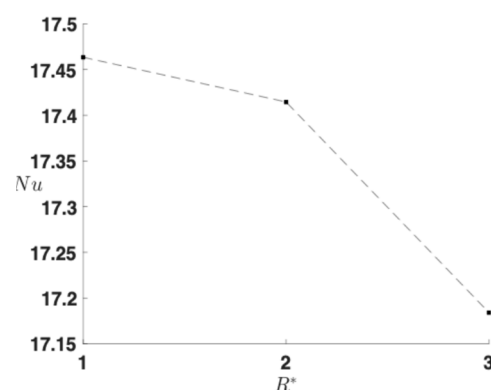| *qoi*	**Grid Refinement**					**Grid Quality**			
	D/100	*D*/200	*D*/400	*R*	p_{obs}	GCI_C	GCI_{32}	GCI_{21}	*C*
Nu	17.1841	17.4146	17.4635	0.2	2.24	2.1%	0.45%	0.09%	0.997

Figure 2. Convergence trend of Nusselt number *Nu* as a function of normalized mesh resolution.

The highest *GCI* error is linked to *Nu*, with an approximate value of 2.1% for the least refined mesh. Furthermore, the *qoi* for all mesh sizes falls within the asymptotic range. This is determined by analyzing the constancy of the asymptotic range, denoted as *C*, shown

in Equation (16), which is approximately equal to one. The coarsest mesh with a size of $D/100$ was chosen for the entire study to minimize computational expenses, based on these findings. The sensitivity of the time-step size is analyzed for the case of $s/D = 0.1$ at $Re_D = 1000$ using three different *CFL* values of 0.125, 0.25, and 0.5, while employing a mesh resolution of $D/100$. The highest error observed was approximately 6.5% for the coefficient of drag (C_D) when the *CFL* number was set to 0.5. All other quantities of interest (*qois*) had errors below 3.5%. The *CFL* value selected for the present study is 0.5 due to this reason.

$$C = r^{pobs} \left(GCI_{21}/GCI_{32} \right) \tag{16}$$

3.2. Validation Results

To validate the results, a two-dimensional simulation of the flow over a solid cylinder was performed for $100 \leq Re_D \leq 1000$ by Alshareef [31]. The mesh cell size and *CFL* number used in the simulation were the same as those mentioned in Section 3.1. The values provided in Figure 1a and Table 3 were assigned to all fluid variables and boundary conditions. Figure 3 displays the temporal evolution of C_D and C_L for $Re_D = 1000$, demonstrating the anticipated periodicity. Figure 4 displays the average values of C_D and Nu as a function of Re_D for the region near the current study Re_D of 500, along with the corresponding benchmark data for airflow over full circular cylinders by Henderson, Fand, and Keswani [36,37]. The data exhibit strong concurrence, indicating that MPM-ICE is a suitable instrument for the proposed slot geometry. The error bands are determined by calculating the maximum discrepancy between the numerical data and each correlation.

Table 3. Initial and boundary conditions.

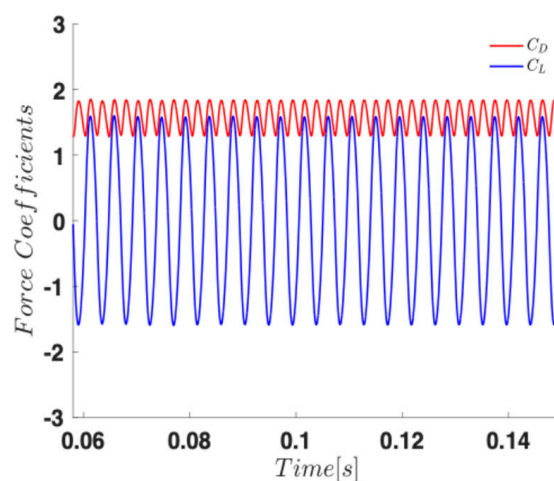| Domain Side	Initial Conditions		Boundary Conditions		
Left			$U_\infty = \frac{v\,Re}{D}$	$T_\infty = 300$ K	$\frac{\partial P}{\partial x} = \frac{\partial \rho}{\partial x} = 0$
Right			$\frac{\partial u}{\partial x} = \frac{\partial \rho}{\partial x} = \frac{\partial T}{\partial x} = 0$	$P = P_{atm}$	
Top and Bottom			$\frac{\partial u}{\partial y} = \frac{\partial P}{\partial y} = \frac{\partial \rho}{\partial y} = \frac{\partial T}{\partial y} = 0$		
Inner	$U_\infty = \frac{v\,Re}{D}$	$T_\infty = 300$ K			
Cylinder	$u = 0$	$T_\infty = 300$ K			

Figure 3. Time history of C_D and C_L for a cylinder in cross flow for $Re_D = 1000$.
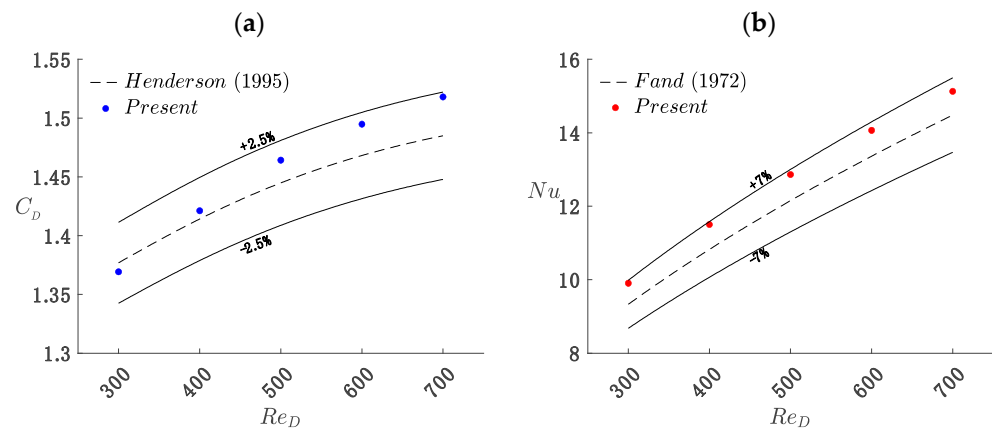
Figure 4. Validation of the numerical results versus benchmark data of a solid cylinder ($s_1 = s_2 = 0$) (**a**) C_D [31] (**b**) Nu [31].

4. Results and Discussion

This section extensively examines the outcomes pertaining to the drag force coefficient, C_D, and heat transfer rate, Q, for V-shaped slots. The variation in the slot width is quantified by the ratio of the slot width to the slot entrance height, denoted as s_2/D. Data for the solid cylinder and slotted cylinder are also provided and compared with data for the proposed V-slot.

4.1. Global Fluid Dynamics Assessment

The flow across the V-shaped cylinder in comparison to the solid cylinder is shown in Figure 5, where the normalized time-averaged velocity magnitude, $V^* = V/V_\infty$, is plotted for the proximity around the cylinder, where x^* and y^* are the normalized coordinates with respect to cylinder diameter. The cases of s_2/D values of 0.1 and 0.125, shown in Figure 5b,c, have a strong resemblance to the solid cylinder, shown in Figure 5a. The flow within the slots for these two cases has a very minimal momentum that affects the downstream region. In addition, looking at the velocity distribution inside the slots for these two cases, the flow seems to be in the fully developed region for the entire length of the slots. When the slot size increases, $s_2/D \geq 0.15$, as shown in Figure 5d–f, the flow within the slots increases, which results in a higher momentum for the jet injected at the slot's exit. This is due to the increase in the flow cross-sectional area and the reduction in the total slot wall, which reduces the viscous shear stress and hence the resistance of the flow. For $s_2/D = 0.15$, the time-averaged V^* within the slot seems to be still in the fully developed regime for the entire slot. Finally, for $s_2/D = 0.2$, the flow distribution illustrates that the flow is in the entry length for the entire slot.

Another interesting observation found is that when the slot size increases, $s_2/D \geq 0.15$, a bulging stagnant region appears at the leading edge at the top and bottom inner walls of s_2. The flow is found to be overshooting a slight distance when the slot size increases where more fluid flow is allowed to enter; however, the new inner stagnation point at the bifurcation region, the tip of the inner cylinder that splits the two slots, causes the fluid to bounce while entering each slot. This causes a permanent time-averaged bulging region, as seen below. The maximum velocity magnitude exceeds that for the free stream only at $s_2/D = 0.2$.

While the time-averaged velocity magnitude figure shows the general flow behavior around the cylinder, one must analyze the instantaneous velocity distribution as well. Figure 6 shows a snippet of the instantaneous velocity distribution for the V-shape slots. When $s_2/D \leq 0.125$, the jet flow exiting the slots creeps around the rear surface due to its low momentum, as shown in Figure 6a,b. This creep flow will result in a lower thermal quality at the rear side of the cylinder, as will be discussed later. In addition, the vortices shed, and the shear layers are in close proximity to the rear side of the cylinder. On the other hand, for $s_2/D \geq 0.15$, the higher momentum of the jet exiting the slot penetrates the

wake region, resulting in an elongation of the wavelength, as shown in Figure 6c–e. This in turn affects the trends in the lift force coefficient, as will be shown below.
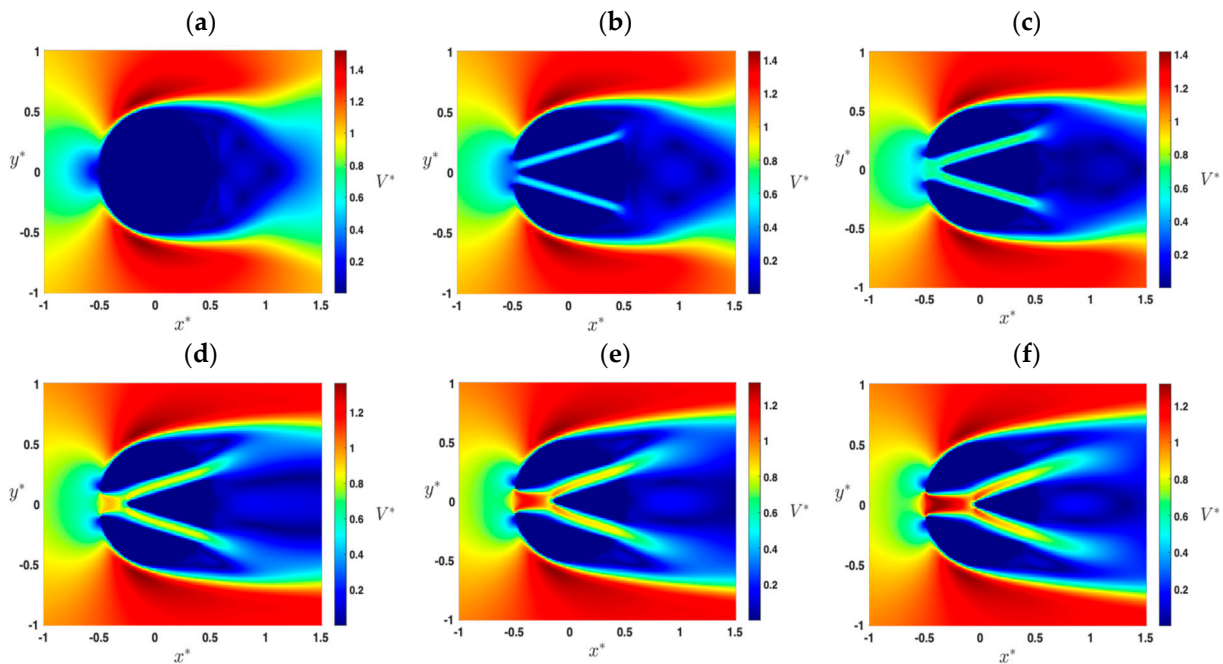

Figure 5. Normalized time-averaged velocity magnitude for (**a**) solid cylinder ($s_1 = s_2 = 0$), (**b**) $s_2/D = 0.1$, (**c**) $s_2/D = 0.125$, (**d**) $s_2/D = 0.15$, (**e**) $s_2/D = 0.175$, and (**f**) $s_2/D = 0.2$.
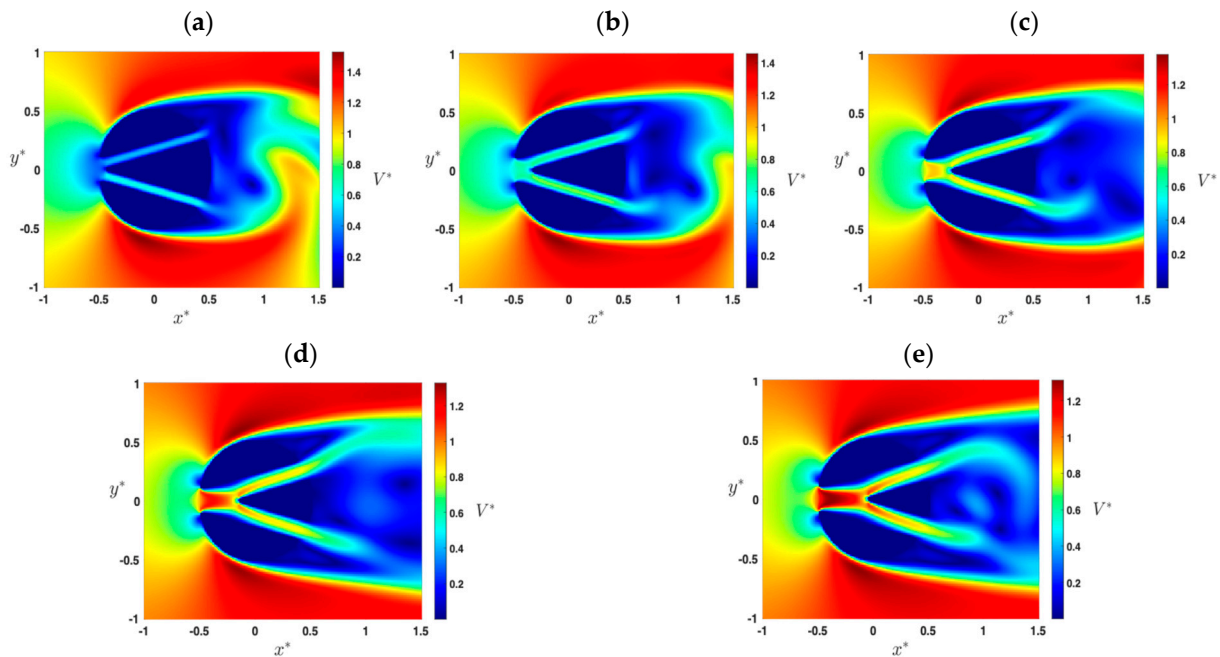

Figure 6. Normalized instantaneous velocity magnitude for (**a**) $s_2/D = 0.1$, (**b**) $s_2/D = 0.125$, (**c**) $s_2/D = 0.15$, (**d**) $s_2/D = 0.175$, and (**e**) $s_2/D = 0.2$.

To qualitatively assess the flow dynamics, the drag and lift coefficients, C_D and C_L, will be addressed. The time history of C_D and C_L based on control volume analysis is shown in Figure 7 as a function of s_2/D. The $s_2/D = 0.1$, 0.125, and 0.15 exhibits a harmonic sinusoidal periodicity in the same fashion as for the solid cylinder. However, the amplitude of the lift coefficient for these cases, as shown below, is lower than the solid cylinder. This is due to the higher momentum of the jet flow exiting the slot as the s_2/D value increases,

which elongates the wake length as discussed earlier, which is in line with the literature findings that relate the cause of a low C_L amplitude to the delay in the separation layer [19]. The lower amplitude of C_L provides a great advantage for structural settings where the vortex-induced vibration *VIV* remains a major concern.
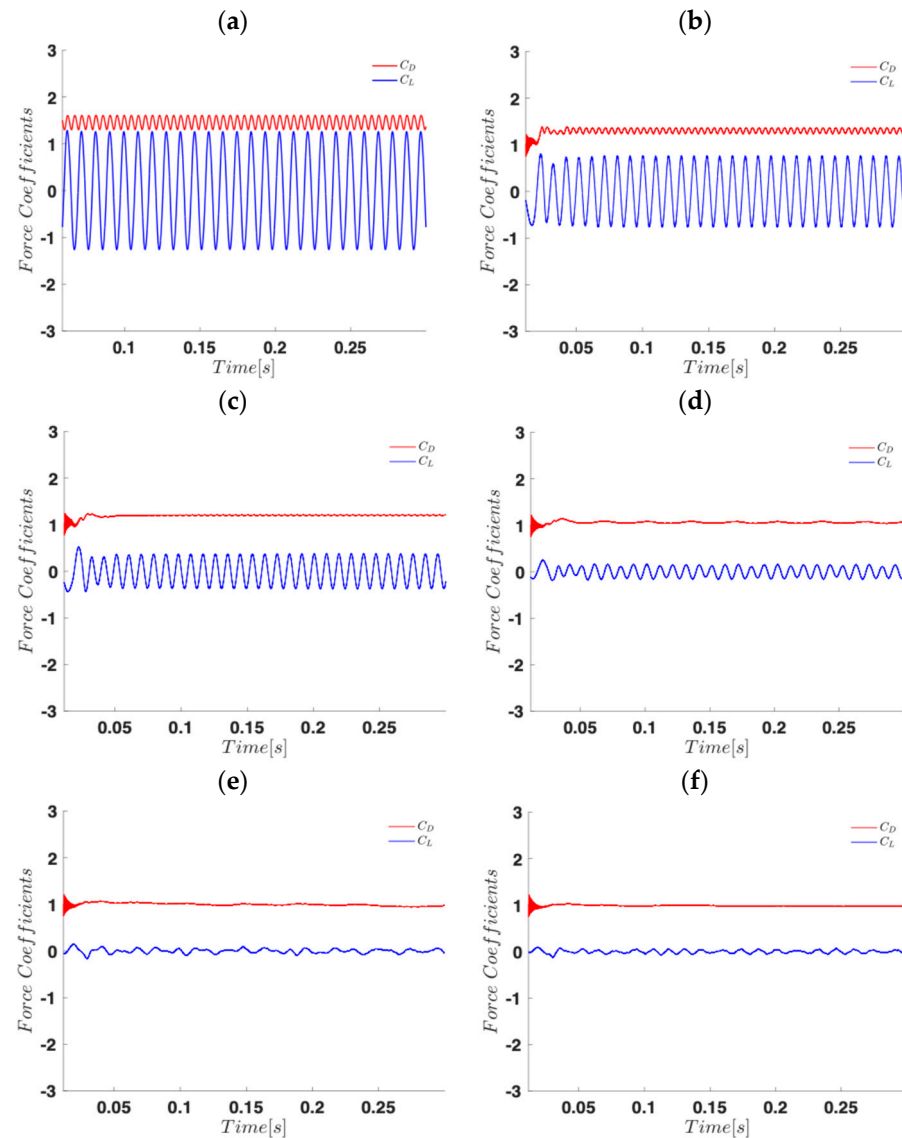

Figure 7. Transient C_D and C_L plots: (**a**) solid cylinder ($S_1 = S_2 = 0$), (**b**) $s_2/D = 0.1$, (**c**) $s_2/D = 0.125$, (**d**) $s_2/D = 0.15$, (**e**) $s_2/D = 0.175$, and (**f**) $s_2/D = 0.2$.

For $s_2/D > 0.15$, C_L exhibits a much lower amplitude; however, the flow becomes more chaotic, and the harmonic periodicity is lost due to the interaction between the jet flow exiting the slot and the vortices shed from the upper and lower curved surfaces of the cylinder. On the other hand, looking at C_D trends, the introduction of the V-shaped slot for all s_2/D values shows a wide range of the total drag reduction in comparison to a solid cylinder with no slot. Despite the substantial surface area increase by the slot, which increases the viscous drag component, cylinders with a V-shape slot experience a lower drag force than the solid cylinder. The drag reduction is attributed to the decrease in the pressure component by increasing the base pressure, which is in parallel with the literature [11–29]. The increase in the base pressure is caused by the interaction of the jet of the slot with the vortices shed; hence, the stagnant fluid is disturbed at the rear side of the cylinder. Even though the jet exiting the flow is angled away from the base of the

cylinder (the rear stagnation point), the interaction with the vortices shed increases the rear pressure, which leads to a lower C_D compared to the solid cylinder case. In addition, like the decreasing trend in the C_L due to the delay of the separation angle, the decreasing trend in the C_D as the s_2/D value increases is directly proportional to the delay in the flow separation angle, where the flow disturbs the stagnant region near the cylinder. This in turn increases the base pressure and hence reduces the total pressure drag force, which is the dominant dynamic horizontal force compared to the viscous shear force. The corresponding time-averaged C_D is 1.306, 1.203, 1.059, 0.982, and 0.979 for s_2/D = 0.1, 0.125, 0.15, 0.175, and 0.2, respectively. The relative reduction in the drag coefficient ranged from ~10% to ~25% between the s_2/D values of 0.1 and 0.2.

4.2. Fluid Dynamics Inside the Slot

The flow field within the slot is elaborated upon quantitively in this section. At the slot entrance, the profiles of the time-averaged normalized x-velocity component, $U^* = U/U_\infty$, as a function of the normalized slot height, $y^* = y/H$, are shown in Figure 8. The profiles exhibit an average symmetry across the slot height. For a lower s_2/D, there is a retardation in the velocity at the center of the slot height which is related to the location of the slot inner stagnation point. Although the slot entrance is fixed for all cases studied, $s_1 = 0.2D$, the inner bifurcation tip that resembles the inner stagnation point is pushed further away from the slot entrance as the s_2/D value increases, which explains the velocity retardation at the center of the slot height. This also explains the larger U^* profiles for larger s_2/D cases, in addition to the reasons discussed earlier (larger cross-sectional flow area and less wall surface area). The reduction in the slot wall surface area for s_2/D = 0.15 and 0.2 relative to s_2/D = 0.1 is 7.3% and 14.8%, respectively.
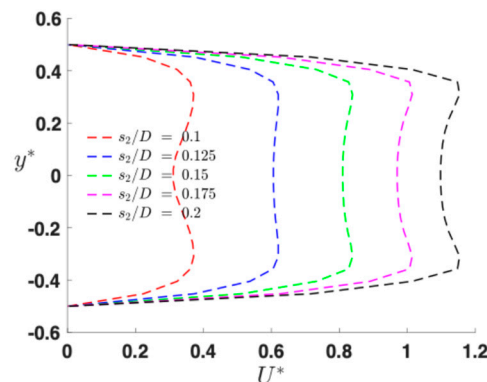

Figure 8. Normalized time-averaged x-velocity component profile at slot entrance.

Normalized x-velocity components, $U^* = U/U_\infty$, across the slot just before the tip of the rear segment, at the bifurcation point, are shown in Figure 9, where two profiles at two different times, $t(C_{L,max})$ and $t(C_{L,min})$, are plotted for s_2/D = 0.1 and 0.125 cases, respectively. The velocity profiles at these two different times show an alternating upward/downward shift due to the flip-flop phenomenon, where the slot jet interaction with the periodic vortex shedding causes the velocity profiles to oscillate. The velocity profile is higher in the upper slot as a reaction to a low-pressure area produced by the vortex aligned with the upper slot exit. This pattern is reversed when the velocity profile is higher in the lower slot. The s_2/D case of 0.1 has a maximum value of $U^* < 1$, as shown in Figure 9a, which results in a creeping flow of the jet toward the rear surface of the cylinder, as discussed earlier and shown in Figure 6. As the s_2/D value increases, the jet has a higher momentum, where $U^* > 1$ resulting in advecting the wake further downstream the cylinder, resulting in a near stagnant area at the cylinder rear surface.
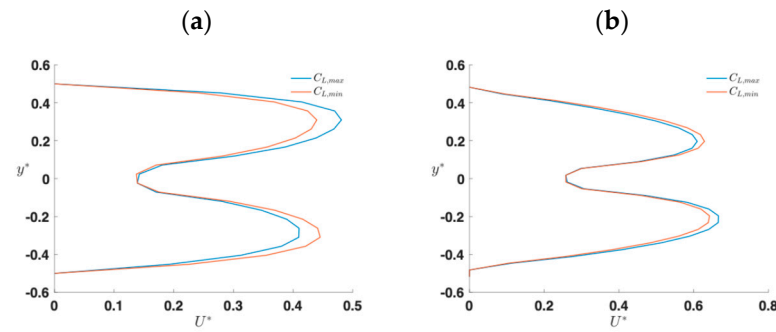
Figure 9. Normalized instantaneous *x*-velocity component profile inside the slot showing the flip-flop phenomenon: (**a**) $s_2/D = 0.1$ and (**b**) $s_2/D = 0.125$.

4.3. Convective Heat Transfer Assessment

The main objective of the proposed fin is to increase the heat transfer surface area. The thermal characteristics of the cases investigated are shown in Figure 10, where the normalized temperature field, $T^* = (T - T\infty)/(Tw - T\infty)$, is plotted in the vicinity of the V-shape slot cylinder. For the smaller slot size, $s_2/D \leq 0.125$, the slot encapsulates a minimal mass flux due to the constricted channel height and excessive viscous flow resistance, as discussed earlier. This leads to a dominantly viscous flow within the slot, where the thermal diffusion dictates the flow, leading to a pseudo creep flow. Hence, the temperature field within the slot is primarily constant in the entire slot region, except in the entrance region. The temperature field in the majority of the slot region is near the cylinder wall temperature, Tw, where the majority of the slot length is in the thermally fully developed region, implying that thermal performance inside the majority of the V-slot area is incompetent. Even though the temperature field is showing a qualitatively lower thermal advantage, the total enhancement in the heat transfer rate in comparison to the solid non-slotted cylinder ranged between 40% and 75% for s_2/D values of 0.1 and 0.125, respectively. This suggests that the thermal enhancement of this magnitude is essentially a result of the heat rates at the entry length of the slots only, as the curved surfaces have lower temperature gradients for the s_2/D value of 0.1 and 0.125 in comparison to the solid cylinder, as seen in Figure 10.
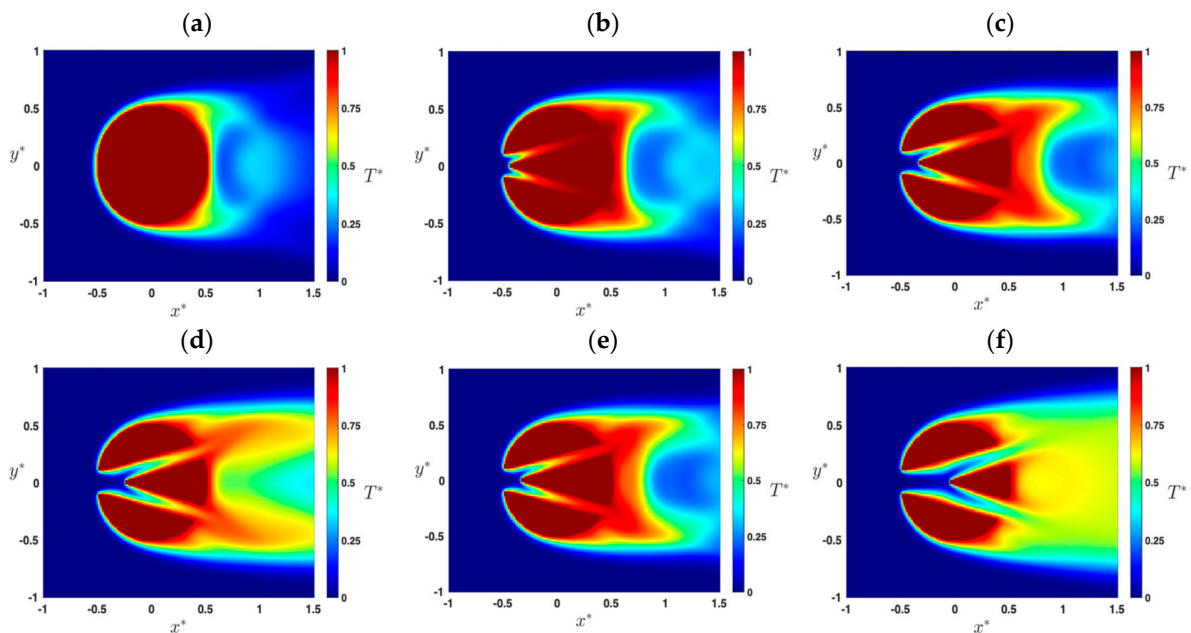

Figure 10. Normalized time-averaged temperature for (**a**) solid cylinder ($s_1 = s_2 = 0$), (**b**) $s_2/D = 0.1$, (**c**) $s_2/D = 0.125$, (**d**) $s_2/D = 0.15$, (**e**) $s_2/D = 0.175$, and (**f**) $s_2/D = 0.2$.

The temperature distribution for $s_2/D \geq 0.15$ shows that the thermal boundary layer is in the developing region, the thermal entry length region, where the heat transfer rates are expected to increase. This is evident by comparing the heat rates for these cases to the heat rate of the solid cylinder where the thermal enhancement was found to be 92%, 91%, and 87% for s_2/D values of 0.15, 0.175, and 0.2, respectively. The thermal enhancement is primarily sourced from the slots, since the curved surfaces do not experience any advantage compared to the solid cylinder. The thermal enhancement peaks at $s_2/D = 0.15$ and then starts to plateau due to the decrease in the total surface area as the s_2/D value increases, regardless of the increase in the slot mass flux. Finally, for the cases of $s_2/D \geq 0.15$, with the thermal boundary layer at the inner top and bottom surfaces, there is a bulging region equal to that found in the velocity field discussed before. This bulging region experiences a lower temperature gradient in comparison to the remaining length of the slot, which is due to the flow slightly overshooting the bulging area in a similar fashion seen in classical diverging tubes, where larger diverging angles result in a recirculation zone.

The overall performance of the V-slot on the drag force and the thermal performance is quantified by the normalized drag force coefficient, $C_D{}^* = C_D/C_{D,solid}$, and the normalized total heat transfer, $Q^* = Q_{V,slot}/Q_{solid}$. $C_{D,solid}$ and Q_{solid} are the drag coefficient and total heat transfer for the solid cylinder. The results of $C_D{}^*$ are presented in Figure 11a, showing a relative drag reduction for all s_2/D cases; however, the reduction for the s_2/D value of 0.2 is not significant. For the V-slot cases with s_2/D values of 0.15 and 0.2, they show a small change in stagnation area displays, and the wake region is almost similar due to a slight reduction in the slot surface area. The results for $C_D{}^*$ for the horizontally slotted cylinder are 0.857, 0.702, and 0.657 for s_2/D values of 0.1, 0.15, and 0.2, respectively. The present results show a slightly smaller drag reduction for s_2/D values of 0.1 and 0.15, but a similar result is obtained for 0.2. The drag reduction caused by the proposed slot shape shows adequate performance compared to other circular fins, as reported in Table 1.
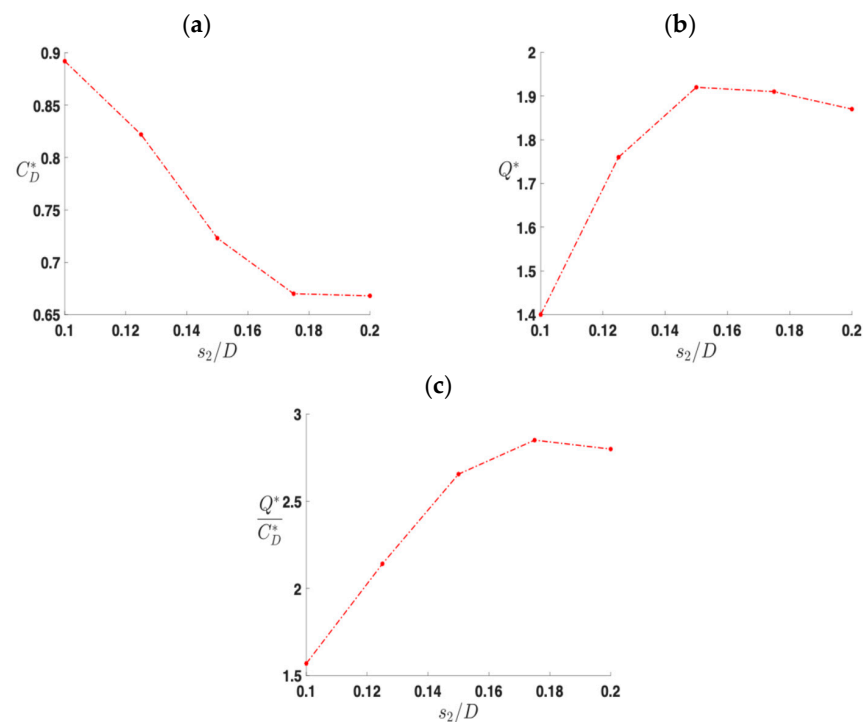

Figure 11. Performance analysis as a function of s_2/D (**a**) $C_D{}^*$, (**b**) Q^*, and (**c**) $Q^*/C_D{}^*$.

The results for Q^* in Figure 11b show that thermal performance is enhanced for all s_2/D cases. However, an optimum heat transfer exists at a s_2/D ratio of 0.15, corresponding to almost double than that of a solid cylinder. Although the heat transfer is proportional to the surface area, the impact of a higher velocity profile on thermal performance surpasses

the surface area reduction for larger slots. In general, the proposed V-slot offers enhanced thermal performance than that reported in Table 1. Compared to Alshareef [31], the V-slot shows a better heat transfer enhancement than horizontal slots where Q^* values are 1.25, 1.48, and 1.57 for the same s_2/D range, i.e., 0.1, 0.15, and 0.2 [31]. Finally, the overall thermal/fluid performance is assessed by taking the ratio of the gained heat rate to the reduction in drag force (Q^*/C_D^*), as shown in Figure 11c. The general performance shows that the optimum performance occurs at $s_2/D = 0.175$.

5. Conclusions

The present work evaluated the drag force and the thermal performance by implementing a V-slot to a circular pin fin in a heat sink device. The objective of the studied configurations was to minimize the drag force by increasing the slot exit width and enhancing thermal performance. The surface area was increased substantially, which allowed two flow passages, and consequently, the heat transfer was improved. Employing a larger slot gap caused a higher flow momentum but reduced the surface area, which led to an optimum heat transfer gain of 92% for $s_2/D = 0.15$ in comparison to a solid circular fin. In addition, and for the same reasons, the proposed slot achieved a lower drag force. The drag reduction contributed from the slot shape was equivalent to other shapes reported in the literature; however, it offers better heat transfer characteristics.

The overall thermal/fluid performance was evaluated by calculating the ratio of the heat gain rate to the decrease in drag force (Q^*/C_D^*), as illustrated in Figure 11. The overall performance indicates that optimal performance is achieved at $s_2/D = 0.175$. Based on a single fin analysis, the present slot design offers an advantage in terms of thermal performance over the solid and slotted cylinders reported in the literature. It opens further examinations on external flow over an array of fins with a leading V-shape slotted cylinder. Another potential work can be on internal flow with multiple V-shape fins in meso- and microscale applications.

Nomenclature

A	Area, m^2
C	Asymptotic range constancy
C_D	Drag coefficient
CFL	Courant-Friedrichs-Lewy number
C_L	Lift coefficient
D	Cylinder diameter, m
e	Internal specific energy, J/kg
F	Force
FS	Safety factor = 1.25

GCI	Grid convergence index
GCI_{coarse}	Coarse mesh $GCI = FS\ r^{pobs}\ |(qoi_1 - qoi_2)/qoi_1|\ /(r^{pobs} - 1)$
GCI_{21}	Fine mesh $GCI = FS\ |(qoi_1 - qoi_2)/qoi_1|\ /(r^{pobs} - 1)$
GCI_{32}	Medium mesh $GCI = FS\ |(qoi_2 - qoi_3)/qoi_2|\ /(r^{pobs} - 1)$
h	Mesh resolution
i	Material index
j	Material index
k	Fluid thermal conductivity, W/(m·K)
L	Length, m
N	Number of materials
Nu	Nusselt number
P	Pressure, Pa
p	Order of accuracy
Pr	Prandtl number
PI	Performance Index
Q	Heat transfer rate, W
qoi	Quantity of interest
r	Grid refinement ratio
R	Monotonic convergence index
$R*$	Normalized grid resolution
Re	Reynolds number
s	Slot width
s/D	Normalized slot width
T	Temperature, K
t	Time, s
$\boldsymbol{u}$	Velocity vector, m/s
U	x-velocity component, m/s
x,y,z	Cartesian coordinate directions
Greek Symbols	
β	Flow incident angle toward the slot
Δx	Cell size in x-direction, m
Δy	Cell size in y-direction, m
Δz	Cell size in z-direction, m
ΔT	$T_w - T_\infty$, K
∞	Free stream
μ	Fluid dynamic viscosity, Pa.s
ρ	Fluid density, kg/m^3
θ	Volume fraction
Subscript	
1	Fine mesh resolution
2	Medium mesh resolution
3	Coarse mesh resolution
21	Fine mesh value
32	Medium mesh value
Coarse	Coarse mesh
cyl	Cylinder
d	Drag
D	Cylinder diameter, m
f	Frontal
max	Maximum value
min	Minimum value
obs	Observed
s	Slot quantity
s/D	Normalized slot width
w	Slot wall
z	Depth in the z-direction, m
Superscript	
*	Normalized value

References

1. Do, K.D.C.; Chung, D.H.; Tran, D.Q.; Dinh, C.T.; Nguyen, Q.H.; Kim, K.Y. Numerical Investigation of Heat Transfer Characteristics of Pin-Fins with Roughed Endwalls in Gas Turbine Blade Internal Cooling Channels. *Int. J. Heat Mass Transf.* **2022**, *195*, 123–125. [CrossRef]
2. Bayomy, A.M.; Saghir, M.Z.; Yousefi, T. Electronic Cooling using Water Flow in Aluminum Metal Foam Heat Sink: Experimental and Numerical Approach. *Int. J. Therm. Sci.* **2016**, *109*, 182–200. [CrossRef]
3. Mudawar, I. Assessment of High Heat Flux Thermal Management Schemes. *IEEE Trans. Compon. Packag. Technol.* **2001**, *24*, 122–141. [CrossRef]
4. Khattak, Z.; Ali, H.M. Air Cooled Heat Sink Geometries Subjected to Forced Flow: A Critical Review. *Int. J. Heat Mass Transf.* **2019**, *130*, 141–161. [CrossRef]
5. Kesavan, D.; Kumar, R.S.; Marimuthu, P. Heat Transfer Performance of Air-cooled Pin-fin Heatsinks: A Review. *J. Therm. Anal. Calorim.* **2022**, *148*, 623–649. [CrossRef]
6. Kheirabadi, A.C.; Groulx, D. Cooling of Server Electronics: A Design Review of Existing Technology. *Appl. Therm. Eng.* **2016**, *105*, 622–638. [CrossRef]
7. Chu, R.C.; Simons, R.E.; Ellsworth, M.J.; Schmidt, R.R.; Cozzolino, V. Review of Cooling Technologies for Computer Products. *IEEE Trans. Devices Mater. Reliab.* **2004**, *4*, 568–585. [CrossRef]
8. Ebadian, M.A.; Lin, C.X. A Review of High-Heat-Flux Heat Removal Technologies. *J. Heat Transf.* **2011**, *133*, 110801. [CrossRef]
9. Agostini, B.; Fabbri, M.; Park, J.E.; Wojtan, L.; Thome, J.R.; Michel, B. State of the Art of High Heat Flux Cooling Technologies. *Heat Transf. Eng.* **2007**, *28*, 258–281. [CrossRef]
10. Nafis, B.M.; Whitt, R.; Iradukunda, A.C.; Huitink, D. Additive Manufacturing for Enhancing Thermal Dissipation in Heat Sink Implementation: A Review. *Heat Transf. Eng.* **2020**, *42*, 967–984. [CrossRef]
11. Ahmed, H.E.; Salman, B.H.; Kherbeet, A.S.; Ahmed, M.I. Optimization of Thermal Design of Heat Sinks: A Review. *Int. J. Heat Mass Transf.* **2018**, *118*, 129–153. [CrossRef]
12. Ran, Y.; Deng, Z.; Yu, H.; Chen, W.; Gao, D. Review of passive control of flow past a circular cylinder. *J. Vis.* **2023**, *26*, 1–44. [CrossRef]
13. Olsen, J.F.; Rajagopalan, S. Vortex Shedding behind Modified Circular Cylinders. *J. Wind Eng. Ind. Aerodyn.* **2000**, *86*, 55–63. [CrossRef]
14. Peng, B.H.; Miau, J.J.; Bao, F.; Weng, L.D.; Chao, C.C.; Hsu, C.C. Performance of Vortex Shedding from a Circular Cylinder with a Slit Normal to the Stream. *Flow Meas. Instrum.* **2012**, *25*, 54–62. [CrossRef]
15. Junwei, W.; Jinwen, Y.; Yi, H.; Feng, B. Experimental Study of Slit Cylinder Vortex Shedding in Circulating Water Channel. In Proceedings of the of 2012 International Conference on Measurement Information and Control, Harbin, China, 18–20 May 2012.
16. Shi, X.D.; Fend, L.H. Control of Flow around a Circular Cylinder by Bleed near the Separation Points. *Exp. Fluids* **2015**, *56*, 214. [CrossRef]
17. Gao, D.L.; Chen, W.L.; Li, H.; Hu, H. Flow around a Slotted Circular Cylinder at Various Angles of Attack. *Exp. Fluids* **2017**, *58*, 132. [CrossRef]
18. Gao, D.L.; Chen, W.L.; Li, H.; Hu, H. Flow around a Circular Cylinder with Slit. *Exp. Therm. Fluid Sci.* **2017**, *82*, 287–301. [CrossRef]
19. Baek, H.; Karniadakis, G.E. Suppressing Vortex Induced Vibrations via Passive Means. *J. Fluids Struct.* **2009**, *25*, 848–866. [CrossRef]
20. Shen, W.J.; Chen, W. Features of Flow past a Circular Cylinder with a Slit. *Sci. Iran. B* **2016**, *23*, 2097–2112.
21. Ma, H.L.; Kuo, C.H. Control of Boundary Layer Flow and Lock on of Wake behind a Circular Cylinder with a Normal Slit. *Eur. J. Mech. B/Fluids* **2016**, *59*, 99–114. [CrossRef]
22. Wang, J.S.; Dong, Y.W. The Numerical Investigation of Flow and Heat Transfer Characteristics of Flow past a Slit Cylinder. *Sci. China* **2017**, *60*, 602–612. [CrossRef]
23. Mahapatra, B.; Ayalasomayajula, S.; Arumuru, V. On the Interaction of Separation Bubbles in the Near Wake of a Cylinder. In Proceedings of the 9th International Symposium on Fluid-Structure Interactions, Flow-Sound Interactions, Flow-Induced Vibration & Noise, Toronto, ON, Canada, 8–11 July 2018.
24. Bao, Z.; Qin, G.; He, W.; Wang, Y. Numerical Investigation of Flow around a Slotted Circular Cylinder at Low Reynolds Number. *J. Wind Eng. Ind. Aerodyn.* **2018**, *183*, 273–282. [CrossRef]
25. Mishra, A.; Hanzla, M.; De, A. Passive Control of the Onset of Vortex Shedding in Flow past a Circular Cylinder using Slit. *Phys. Fluids* **2020**, *32*, 013602. [CrossRef]
26. Cheng, X.; Wu, H. Heat Transfer Enhancement for Wake Zone Using Slit Pillar in Micro channel Hear Sinks. *J. Heat Transf.* **2020**, *142*, 012502. [CrossRef]
27. Jadon, L.; Arumuru, V. Numerical Investigation on Heat Transfer and Flow Characteristics of a Confined Circular Cylinder with Slit. *J. Therm. Sci. Eng. Appl.* **2020**, *12*, 051007. [CrossRef]
28. Hsu, L.C.; Liang, C.W. Heat Transfer in Flow Past Two Cylinders in Tandem and Enhancement with a Slit. *Energies* **2021**, *14*, 308. [CrossRef]

29. Alshareef, S.; Harman, T.; Ameel, T. Thermal Fluid Assessment of Cylinders with Multiple Slots in Aligned Flow. In Proceedings of the 1st IEEE Intersociety Conference on Thermal and Thermomechanical Phenomena in Electronics Systems (iTherm), San Diego, CA, USA, 31 May 2022–3 June 2022.

30. Alshareef, S.; Harman, T.; Ameel, T. Thermal Fluid Assessment of Bluff Versus Streamlined Bodies with a Slot for Aligned Flow. In Proceedings of the ASME Heat Transfer Summer Conference, Philadelphia, PA, USA, 11–13 July 2022.

31. Alshareef, S.; Harman, T.; Ameel, T. Fluid dynamic and thermal performance of a slotted cylinder at low Reynolds number. *Int. J. Heat Mass Transf.* **2023**, *212*, 124268. [CrossRef]

32. Guilkey, J.E.; Harman, T.; Banerjee, B. An Eulerian Lagrangian Approach for Simulating Explosions of Energetic Devices. *Comput. Struct.* **2007**, *85*, 660–674. [CrossRef]

33. Faucett, A.; Harman, T.; Ameel, T. Computational Determination of the Modified Vortex Shedding Frequency for a Rigid, Truncated, Wall-Mounted Cylinder in Cross-Flow. In *Proceedings of IMECE2014*; Taylor & Francis: Philadelphia, PA, USA, 1998; pp. 23–40.

34. van Rij, J.; Harman, T.; Ameel, T. Slip Flow Fluid Structure Interaction. *Int. J. Therm. Sci.* **2012**, *58*, 9–19. [CrossRef]

35. Roache, P.J. Perspective: A Method for Uniform Reporting of Grid Refinement Studies. *J. Fluids Eng.* **1994**, *116*, 405–413. [CrossRef]

36. Henderson, R.D. Details of the Drag Curve near the Onset of Vortex Shedding, Phys. *Fluids* **1995**, *7*, 2102–2104. [CrossRef]

37. Fand, R.M.; Keswani, K.K. A Continuous Correlation Equation for Heat Transfer from Cylinders to Air in Crossflow for Reynolds number from 10^{-2} to $2\text{x}10^5$. *Int. J. Heat Mass Transf.* **1972**, *15*, 559–562. [CrossRef]